frontiers in Earth Science

ORIGINAL RESEARCH
published: 17 May 2021
doi: 10.3389/feart.2021.653672

High-Resolution 3D Seismic Imaging of Fault Interaction and Deformation Offshore San Onofre, California

James J. Holmes[1], Neal W. Driscoll[1] and Graham M. Kent[2]*

[1] Scripps Institution of Oceanography, UC San Diego, La Jolla, CA, United States, [2] Nevada Seismological Laboratory, University of Nevada, Reno, NV, United States

The Inner California Borderland (ICB) records a middle Oligocene transition from subduction to microplate capture along the southern California and Baja coast. The closest nearshore fault system, the Newport-Inglewood/Rose Canyon (NIRC) fault complex is a dextral strike-slip system that extends primarily offshore approximately 120 km from San Diego to Newport Beach, California. Holocene slip rates along the NIRC are 1.5–2.0 mm/year in the south and 0.5 mm/year along its northern extent based on trenching and well data. High-resolution 3D seismic surveys of the NIRC fault system offshore of San Onofre were acquired to define fault interaction across a prominent strike-slip step-over. The step-over deformation results in transpression that structurally controls the width of the continental shelf in this region. Shallow coring on the shelf yields a range of sedimentation rates from 0.27–0.28 mm/year. Additionally, a series of smaller anticlines and synclines record subtle changes in fault trends along with small step-overs and secondary splay faults. Finally, sedimentary units onlapping and dammed by the anticline, place constraints on the onset of deformation of this section of the NIRC fault system. Thickness estimates and radiocarbon dating yield ages of 560,000 to 575,000 years before present for the onset of deformation.

Keywords: Newport-Inglewood-Rose Canyon fault system, continental shelf, tectonics, San Onofre, 3D seismic acquisition, fault interactions, geomorphology

OPEN ACCESS

Edited by:
Paola Vannucchi,
University of Florence, Italy

Reviewed by:
Andrea Zanchi,
University of Milano-Bicocca, Italy
Luigi Jovane,
University of São Paulo, Brazil
Eli Silver,
University of California, Santa Cruz, United States

****Correspondence:***
James J. Holmes
jjholmes@ucsd.edu

Specialty section:
This article was submitted to Structural Geology and Tectonics, a section of the journal Frontiers in Earth Science

Received: *14 January 2021*
Accepted: *15 April 2021*
Published: *17 May 2021*

Citation:
Holmes JJ, Driscoll NW and Kent GM (2021) High-Resolution 3D Seismic Imaging of Fault Interaction and Deformation Offshore San Onofre, California. Front. Earth Sci. 9:653672. doi: 10.3389/feart.2021.653672

INTRODUCTION, GEOLOGIC BACKGROUND, AND MOTIVATION

Prior to the late Oligocene/early Miocene, the western margin of North America was dominated by Farallon plate subduction (Lonsdale, 1991; Crouch and Suppe, 1993; Bohannon and Parsons, 1995). The cessation of subduction ushered in a complex tectonic sequence involving block rotation, extension, and then an eventual switch to a transform margin, dominated by the dextral strike-slip San Andreas Fault (e.g., Legg, 1991; Crouch and Suppe, 1993; Nicholson et al., 1994; Bohannon and Geist, 1998). In southern California, the San Andreas Fault (SAF) accommodates approximately 18–22 mm/year of slip between the Pacific and North American tectonic plates (Lindsey and Fialko, 2013). Not all of the slip, is accommodated by the SAF, San Jacinto (SJF) and Elsinore (EF) systems. Roughly 5–8 mm/year of the relative plate motion is being taken up by offshore strike-slip fault systems (Bennett et al., 1996; Platt and Becker, 2010; Maloney et al., 2016).

The Inner California Borderland (ICB) (**Figure 1B**) is a region marked by tectonic deformation offshore southern California and northern Baja that records a middle Oligocene transition from a subduction regime to microplate capture (Bohannon and Geist, 1998). Since the late Miocene

to early Pliocene, the margin has been dominated by right-lateral strike-slip faulting, often on reactivated Mesozoic structures (Hill, 1971; Grant and Shearer, 2004). These faults account for approximately 10% of the total slip between the North America and Pacific plates (DeMets and Dixon, 1999; Platt and Becker, 2010).

The Newport-Inglewood/Rose Canyon (NIRC) fault complex, located closest to shore, is a right-lateral strike-slip system extending from Old Town, San Diego (Rockwell, 2010) to the Cheviot Hills in the Los Angeles Basin (Barrows, 1974). Offshore segments extend approximately 120 km from La Jolla Cove to the San Joaquin Hills near Newport Beach, California (Sahakian et al., 2017). The Holocene slip rate is 1.5–2.0 mm/year along the southern onshore extension of the fault based on paleoseismological studies (Lindvall and Rockwell, 1995) and 0.35–0.55 mm/year along its northern onshore extent based on cone penetration tests (CPTs; Grant et al., 1997) and well data (Freeman et al., 1992). The fault system is composed of segments belonging to two subsystems: the Newport-Inglewood fault system (NIFZ) terminating in the Los Angeles basin in the north, and the Rose Canyon fault system (RCFZ) starting near Downtown San Diego in the south. The two systems interact and transition between each other at a leftward step-over near Carlsbad Canyon (labeled "CC" in **Figure 1B**; Ryan et al., 2009). Recent geophysical and geological studies of the fault zone reveal the offshore fault system is comprised of four major segments separated by three step-overs (Sahakian et al., 2017).

In the region offshore of San Onofre, the Camp Pendleton splay of the Northern strand interacts with the Carlsbad Canyon strand, following the naming convention of Sahakian et al. (2017). Step-over widths between these strands are all 2 km or less (**Figure 1B**; Sahakian et al., 2017). Models and empirical data reveal that an earthquake rupturing the entire offshore length of the NIRC system, could produce an Mw 7.0–7.3 earthquake (Sahakian et al., 2017).

In general, fault geometry and interactions along the NIRC fault system offshore of San Onofre remain poorly constrained compared to the onshore strands (Ryan et al., 2009; Sahakian et al., 2017). Seismicity also seems to be focused onshore, being relatively diffuse offshore (**Figure 1B**; Fischer and Mills, 1991; Grant and Shearer, 2004). The most recent large seismic events on the fault complex occurred onshore near the ends of the fault system—the 1933 Long Beach Earthquake (Mw 6.4) to the north, and a paleoseismological event dated AD 1650 $\pm$ 120 years near La Jolla, CA, United States (Lindvall and Rockwell, 1995; Rockwell, 2010).

Fault segments and step-over widths interact to permit or inhibit through-going rupture and act as controls on the maximum possible magnitude of the consequent earthquake. They are important inputs into models of ground motion. Wesnousky (2006) compiled the properties of 22 historical earthquakes and found that, regardless of the tectonic regime involved (strike-slip, normal, and reverse faulting) the probability of a through-going rupture was higher for a step-over with a width of less than 3–4 km. Sahakian et al. (2017) analyzed re-processed industry 2D multichannel seismic reflection (MCS) profiles acquired along the length of the offshore NIRC system and found a 30–40% possibility of end-to-end rupture on the main segments based on static coulomb stress models. Previous studies have shown a lack of Holocene sediment displacement in offshore segments between Dana Point and Oceanside (Klotsko et al., 2015; Sahakian et al., 2017; Singleton et al., 2019). It is possible that changes in fault geometry and step-over width along NIRC actually act as a barrier to through-going ruptures on this system (Sahakian et al., 2017).

In several places along the coast, multiple strands strike adjacently to each other (Ryan et al., 2009; Sahakian et al., 2017), adding complexity to models of major NIRC strands rupturing together. Recent studies of multi-fault earthquake propagation, as observed in the recent 2016 Kaikōura Earthquake in New Zealand (Clark et al., 2017; Hamling et al., 2017; Kaiser et al., 2017; Stirling et al., 2017), revealed complex and cascading fault linkages that control rupture lengths and potential earthquake magnitudes.

Advances in high-resolution geophysical imaging provide higher resolution of offshore deformation and fault architecture; such technological developments allow for improved imaging of near-vertical fault segments, offsets at step-overs, and fault recency (Kluesner and Brothers, 2016; Nishenko et al., 2018). Near-vertical faults can be imaged in three-dimensional seismic data because the offset is projected onto the time-slice (i.e., map view). In addition, the density of data provides information on how fault-fold propagation occurs.

Recent work in the region has documented a leftward step in the NIRC fault located at the widest part of the continental shelf. We were thus motivated to conduct our survey of this region for two reasons: first and foremost, we sought to understand fault interaction at step-overs along this portion of the shelf. The second reason was to image offset channels that appear structurely controlled to constrain slip-rate along fault segments of the NIRC system, and understand better how these fault systems interact both surficially and at depth.

Wesnousky's (2006) empirical data is surficial and doesn't image fault structure at depth. Sahakian examined fault segments both surficially and at depth (Sahakian et al., 2017). Their 2D MCS data was sufficient to map the morphologic expression of the anticline colocated with the step-over; however, the density and resolution of the data were not sufficient to understand the details of the step-over and fault-fold interaction. Seismic imaging in 3D allows us to unravel the complexity in greater detail; imaging the Earth at the scale of the deformation.

Here we present recently acquired 3D P-Cable seismic reflection data to define NIRC fault segment geometry, segment interaction and attendant deformation at a large step-over ($\sim$2.8 km). In addition, we provide evidence that fault segment interaction along this portion of the margin also appears to control the width of the margin, sequestering of sediments on the shelf, and divergence of off-shelf drainage systems.

MATERIALS AND METHODS

3D MCS Acquisition and Processing

For several decades, the benefits of using 3D MCS imaging to study offshore architecture have been employed in regions such

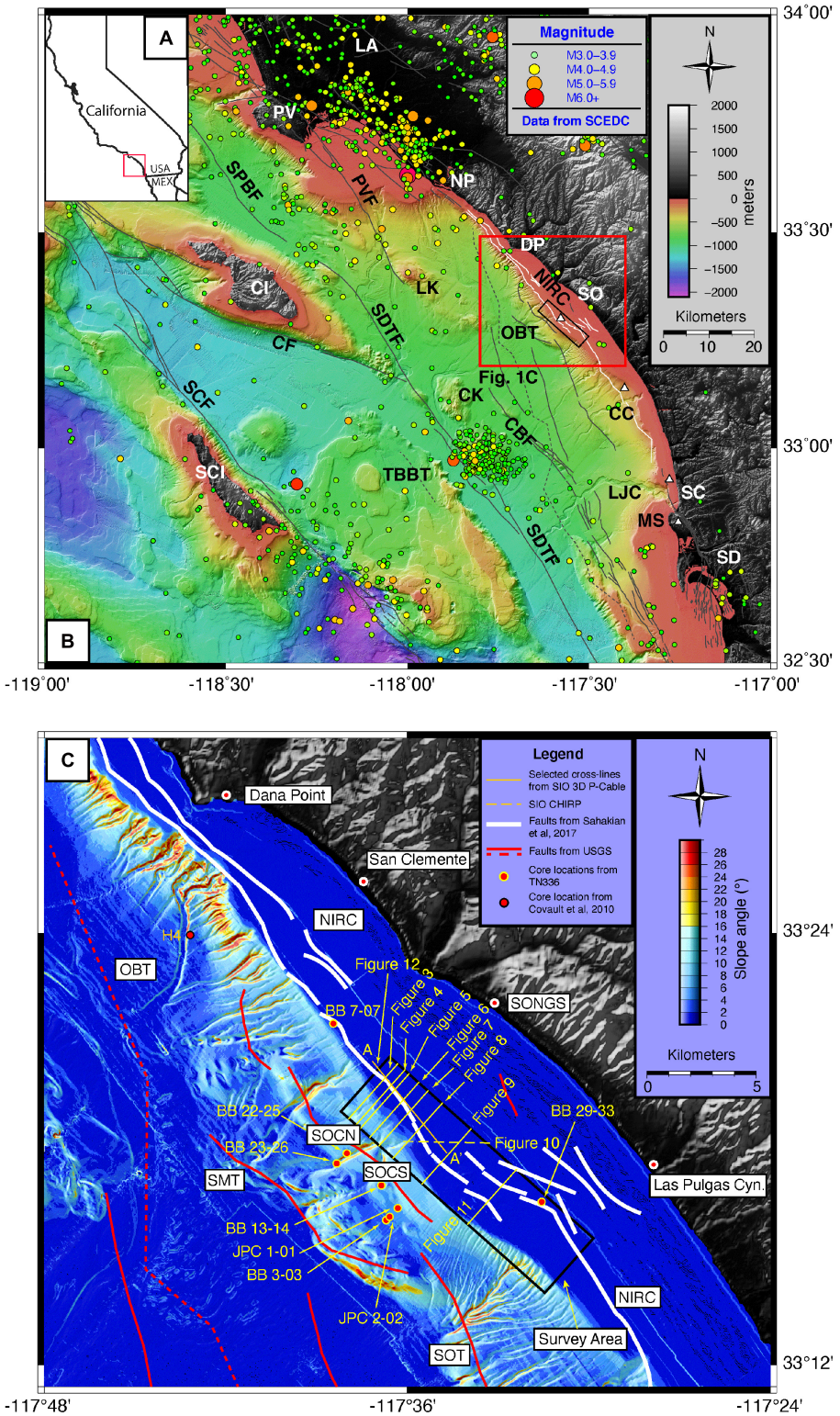

FIGURE 1 | (A) Regional map of California State showing the location of the Inner California Borderland – red box. **(B)** Area map of Inner California Borderland (ICB) relative to the southern California coast with historical seismicity data represented by colored circles. Seismicity data are from the Southern California Earthquake Data Center (SCEDC). Major fault systems are traced in solid black, with the exception of the Newport-Inglewood Rose Canyon (NIRC) fault system, traced in solid white. Red box outlines area shown in **(C)**. Black rectangle outlines the survey area. Scale for topography and bathymetry is shown. Dashed faults denote possible blind thrusts. White triangles denote approximate location of "pop-up" compressional structures due to leftward stepping of the fault strands. Major fault

(Continued)

FIGURE 1 | Continued
systems are labeled. **(C)** Location map of survey area off San Onofre and coastal communities of Dana Point and San Clemente. Location of Las Pulgas Road within Marine Corps Base Camp Pendleton is also shown. Survey area bounds on continental shelf are outlined with a black rectangle. Shown here in white are segments of the Newport-Inglewood Rose Canyon (NIRC) fault system from Sahakian et al. (2017). Solid and dashed red fault segments from USGS Fault and Fold database (U.S. Geological Survey [USGS] and California Geological Survey [CGS], 2006). Yellow solid lines within the survey box denote locations of crosslines and arbitrary line shown in the figures. Yellow dashed line represents path of SIO CHIRP line displayed in **Figure 10**. Also shown are sampled core locations from TN336 cruise. Cores prefixed "BB" are gravity cores. "JPC" are jumbo piston cores. "H4" is location of piston core from Covault et al. (2010). Bathymetry from Dartnell et al. (2015). CBF, Catalina Basin Fault; CC, Carlsbad Canyon; CF, Catalina Fault; CI, Catalina Island; CK, Crespi Knoll; DP, Dana Point; LA, Los Angeles; LJC, La Jolla Canyon; LK, Lasuen Knoll; MS, Mount Soledad; NIRC, Newport-Inglewood Rose Canyon Fault; NP, Newport; OBT, Oceanside blind thrust; PV, Palos Verdes; PVF, Palos Verdes Fault; SC, Scripps Canyon; SCF, San Clemente Fault; SCI, San Clemente Island; SD, San Diego; SDTF, San Diego Trough Fault; SO, San Onofre; SOCN, San Onofre Canyon North; SOCS, San Onofre Canyon South; SPBF, San Pedro Basin Fault; TBBT, Thirtymile Bank blind thrust.

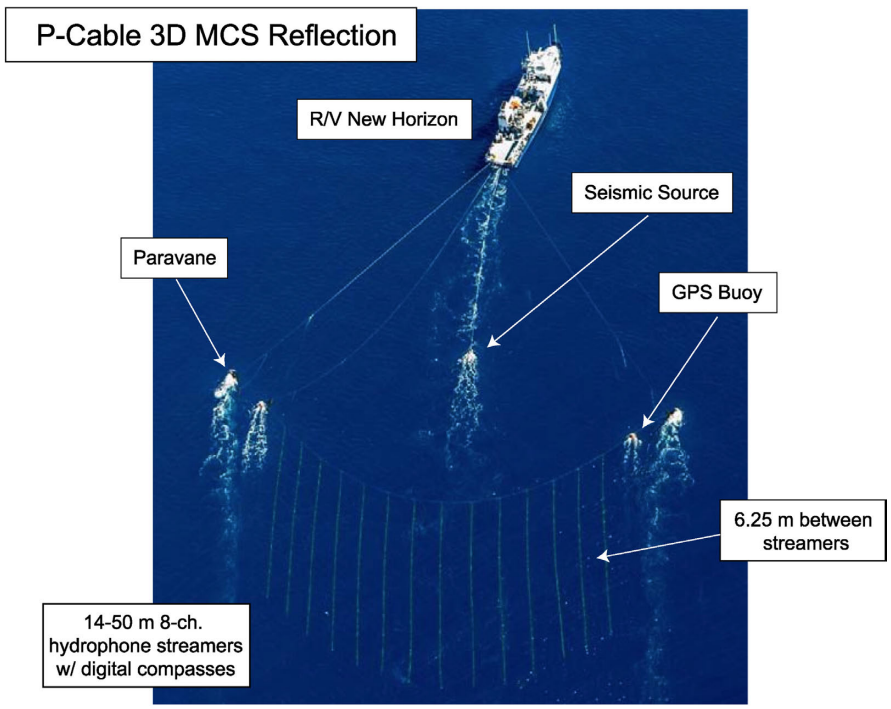

FIGURE 2 | Aerial photo of Scripps Institution of Oceanography's Research Vessel New Horizon towing the *P*-Cable 3D Multichannel Seismic Reflection System, with major components of system labeled.

as Costa Rica (Edwards et al., 2018), Japan (Gulick et al., 2010), and New Zealand (Eberhart-Phillips and Bannister, 2010; Morley et al., 2017; Morley, 2018). Recently, portable state-of-the-art 3D seismic reflection systems, such as the 3D P-Cable system, have been developed that can be deployed from Ocean-Class research vessels of choice (Ebuna et al., 2013; Eriksen et al., 2015). P-Cable employs a cross-cable that is kept under tension by two one-ton paravanes attached to the ends of the cross-cable and to the stern (port and starboard) when the vessel is underway (**Figure 2**). Attached to the cross-cable are fourteen 50 m long streamers, each containing 8 hydrophones, with digital compasses and depth sensors at the head and end of each streamer. Short streamers allow for greater operational maneuverability during acquisition; they also reduce anti-aliasing artifacts, allowing for greater resolution after processing (Brookshire et al., 2016). Differences in hydrophone position caused by the camber of the cross-cable are tracked using a set of GPS transmitters positioned at various points on the system: on the vessel, at the ends of the cross-cable, on the paravanes, and on the seismic source. Tracked changes in system geometry are then corrected during processing.

In late summer/fall 2013, we collected 2D seismic reflection data on the R/V New Horizon (NH1320), which was then processed and analyzed to assist in selecting locations for a later focused 3D survey. Guided by our 2D data observations, we acquired the first high-resolution 3D data set of the offshore NIRC fault segments in the survey area (**Figures 1B,C**) using P-Cable (survey acquisition parameters are listed in **Supplementary Material**) towed from the stern of New Horizon (NH1323). Our survey area, a 54.2 km^2 grid with coverage over the continental shelf and shelf-break, was targeted to maximize imaging of the NIRC fault system in a region where the shelf widens anomalously compared to the trend of narrow shelf width between La Jolla and the San Pedro Shelf south of Long Beach (**Figure 1C**).

Mapped drainage channels also were targeted, as they would provide piercing points across the NIRC fault system to constrain slip. The survey data were acquired in depths ranging from 50–100 m with 3D bin sizes of 3.125 m. A triple-plate boomer operating at 1.8 kJ was selected as the acoustic source for the continental shelf because of its high-resolution at relatively shallow water depths.

We measured a peak frequency of 175 Hz (full frequency response graph shown in **Supplementary Figure 1**), allowing us a minimum vertical resolution of 2.1 m. Oscillations produced by the boomer seismic source (termed the "Bubble Effect") manifested in the data as a very thick series of strong parallel reflections near the seafloor. Despite post-stack deconvolution during initial processing, the reverberation effect still effectively masks real reflection features in the top of the seismic section, with the result of obscuring feature resolution at shallow depths down 15 ms (11 m) from the seafloor. This problem has also been noted on previous P-Cable surveys conducted with AP3000 boomer sources (Pacific Gas and Electric Company [PG & E], 2014).

A 1000 ms record length was digitized, and after processing the reflections were resolved to 800 ms. Much of the analysis of the data was performed between 100 and 400 ms two-way travel time, where data resolution and imaging were optimum. Complete acquisition parameters are described in the processing report included in **Supplementary Material**.

We collaborated with Geotrace Technologies, a petroleum services company, to process and compile the data into both amplitude-attribute and similarity-attribute products for interpretation. The amplitude volume allows easy identification of reflections across subsurface stratigraphy based on the relative impedance contrast (i.e., the product of density and velocity) of acoustic reflectors in a trace.

The similarity attribute assigns a value to a bin based on the correlation between the waveform and amplitude of two or more different traces. This attribute is computed as the normalized cross-correlation of all bins within a specified 3D grid (Bahorich and Farmer, 1995). In such a volume, a correlative value of 1 represents the state of "perfectly similar," while a value of 0 represents the state of "completely dissimilar." Similarity attribute volumes are ideal for looking at large-scale discontinuities, such as sharply dipping beds, faults, and paleochannels. These features become readily interpretable especially in the context of an isochron (a "time-slice") view. In amplitude data, these features can often be obscured if they run parallel to strike in a given time-slice. The amplitude volume is instead most useful in vertical profiles, where fault presence and character can be easily identified by analyzing stratigraphic package displacement.

Additional in-house filtering was applied to both the amplitude and similarity data volumes, following a workflow described by Kluesner and Brothers (2016), to increase reflector continuity and facilitate data interpretation (**Supplementary Figure 2**). A parameterized dip-steered median filter was applied to each volume in order to reduce random noise. The resulting noise from the filtering process was isolated prior to removal and evaluated for efficacy and potential removal of signal. Finally, a dip-steered diffusion filter was applied to each volume with a symmetric step-out (8×8 for the amplitude volume, and 6×6 for the similarity volume) in both inline and crossline directions and a 0 ms time-gate parameter. This filtering workflow removed randomized noise and enhanced discontinuities to improve fault identification, which increased confidence in our interpretations.

A number of additional seismic attribute volumes were generated using the original amplitude data, in order to facilitate seismic interpretation in specific cases. Attribute analysis has proven to be a very useful tool for geophysicists in the detection and enhancement of fault traces, and paleochannels, as well as illuminating structural details (Kalid et al., 2016). Additional seismic attribute volumes were generated to assist interpretations. These included attributes calculated from geometric properties such as curvature, that greatly improved mapping of structures and paleochannels (Roden et al., 2015).

All of our interpretations were iteratively made by using arbitrary lines, as well as vertical dipline/strikeline profiles, to identify structures and faults in vertical profiles of the amplitude data. Next, we confirmed our initial interpretations in similarity attribute time-depth slices and correlated our results with other seismic attributes. Finally, we returned to the vertical profiles with our interpretations, to further constrain fault length and character. Although we did not depth migrate our 3D volumes due to a lack of well control, we adopted the following velocity function described by Ryan et al. (2009) to calculate depths for estimations in this paper:

$$V = 1500 + 0.2438t + 8.2659 - 10^{-5}t^2$$

Where V represents interval velocities in meters per second, and t represents two-way subsurface travel time (TWTT) in milliseconds. This function was derived using interval velocities measured from 2D MCS profiles during Jebco cruise J188SC (Mineral Management Service [MMS], 1997; Triezenberg et al., 2016), including profiles that crossed our survey areas.

Mapping of some paleochannels was accomplished by computing the most negative and most positive curvature seismic attributes on the original data volume (Roberts, 2001). This imaging method was most successful at revealing paleochannels on the western and eastern edges of the survey area where distortion due to fault damage was minimal.

Age Control

In order to constrain onset of deformation, we radiocarbon dated organic material recovered in cores. The shelf and slope near San Onofre have not been well-sampled. Conrad et al. (2018), however, mapped the Quaternary boundary in the region using unpublished industry well data acquired as part of the Caldrill program in the 1970s and now held by the United States Bureau of Safety and Environmental Enforcement (Conrad et al., 2018).

In January 2016, 64 Gravity (GC) and Jumbo-Piston Cores (JPC) were collected onboard the R/V Thomas G. Thompson (TN336) as part of a regional study designed to provide age constraints on shelf/slope evolution, and recent faulting. We selected possible piercing points, such as faults and paleochannels, as coring targets using previously collected

multichannel seismic and CHIRP data. JPC trigger cores were also acquired and logged. In some cases, positional drift caused the cores to be slightly offset from the profiles, in which case the core locations were projected orthogonally onto the profile. Once on-board, we analyzed intact cores for magnetic susceptibility, gamma density, P-wave velocity, and resistivity using a GeoTek Core-logger. Cores were then split and observations of color, grain size, sediment structures, and general lithology were recorded.

We selected fourteen samples for radiocarbon dating due to proximity to the survey area. Ten of those samples were analyzed at the National Ocean Sciences Accelerator Mass Spectrometry facility at the Woods Hole Oceanographic Institution (WHOI) and produced an age using the Libby half-life of 5568 years and following the convention of Stuiver and Pollach (1977). The W.M. Keck Carbon Cycle Accelerator Mass Spectrometry facility at the University of California, Irvine (UCI) analyzed the other four samples following the same conventions. ^{14}C ages were calibrated using the CALIB program, version 7.0.4 (Stuiver and Reimer, 1993). Non-fragmented planktonic foraminifera that had not undergone diagenesis were preferentially collected.

Ages of planktonic foraminifera of less than 12,000 years were calibrated with a reservoir age of 800 years. We used a reservoir age of 1,100 years for planktonic foraminifera >12,000 years (Southon et al., 1990; Kienast and McKay, 2001; Kovanen and Easterbrook, 2002) and 1,750 years for a benthic reservoir age similar to Covault et al. (2010). For cores containing more than two dates, we used these reservoirs as a parameter to generate age-depth models with the Bacon age-modeling software, version 2.3.3 (Blaauw and Christen, 2011). A more exhaustive description of measurements performed on these cores is documented by Wei et al. (2019).

Of the fourteen tested samples, two are from short gravity cores collected on the continental shelf, and the rest were acquired on the continental slope directly southwest of the survey area (**Figure 1C**). Two samples, both acquired on the slope below the widest part of the shelf, are greater than 52,000 years old and thus eliminated as radiocarbon dead. Based on analysis of the remaining samples, we calculated the sedimentation rates (**Table 1**). Sedimentation rates were highly variable, based on sample depth and core location. Cores sampled from the widest part of the continental slope showed extremely low sedimentation rates. The highest sedimentation rates were computed on cores that were taken within drainage channels or on the continental shelf.

Covault et al. (2010) published a sedimentation rate of 0.33 mm/year for their piston core "H4," located at the toe of the continental slope approximately 10 km northwest of our survey area, at a sample depth of 374–384 cm. As sediment depositional regimes tend to vary from shelf to slope to abyssal plain, we calculated a sedimentation rate from gravity core BB 29–33 that was collected within the bounds of the survey area on the continental shelf. We sampled between 36 and 44 cm depth. Radiocarbon testing returned an age of 1,460 years with an error of 20 years. Using that value, we calculated a sedimentation rate range of 0.27 to 0.28 mm/year. Although the core was sampled near the bottom, the core length is

TABLE 1 | TN336 Cores, radiocarbon ages, and sedimentation rates.

Core ID	Sample Depth (cm)	Description	Calibrated Radiocarbon Age (years)	Age Error (years)	Minimum Sedimentation Rate (mm/year)	Maximum Sedimentation Rate (mm/year)	Testing Laboratory
BB 3-03	165–170	Planktonic foraminifera	16,300	50	0.103	0.103	WHOI
BB 7-07	26–30	Planktonic foraminifera	2,950	20	0.094	0.096	WHOI
BB 13-14	17–21	Planktonic foraminifera	40,000	960	0.005	0.005	WHOI
BB 13-14	39–43	Planktonic foraminifera	Too old	–	–	–	WHOI
BB 22-25	133–137	Planktonic foraminifera	22,944	78	0.059	0.059	UCI
BB 22-25	256–260	Planktonic foraminifera	38,700	910	0.065	0.068	WHOI
BB 23-26	127–131	Planktonic foraminifera	9,180	25	0.140	0.141	WHOI
BB 23-26	210–214	Planktonic foraminifera	9,840	30	0.215	0.216	WHOI
BB 29-33	36–44	Planktonic foraminifera	1,460	20	0.270	0.278	WHOI
JPC 1-01	15–19	Benthic foraminifera	7,880	25	0.019	0.019	WHOI
JPC 1-01	185–189	Benthic foraminifera	19,950	90	0.092	0.093	WHOI
JPC 2-02	43–47	Planktonic foraminifera	18,043	69	0.025	0.025	UCI
JPC 2-02	157–161	Planktonic foraminifera	39,347	395	0.040	0.041	UCI
JPC 2-02	230–234	Planktonic foraminifera	Too old	–	–	–	UCI

only 47 cm. Due to the shallow sampling, extrapolating the sedimentation rate to several hundred meters depth introduces much uncertainty.

RESULTS

Deformation and Fault Characterization

A series of stair diagrams are presented to highlight the three-dimensional architecture of the NIRC fault segments and attendant deformation (**Figures 3–9**, **11**). A stair diagram is a visual depiction of 3D seismic data combining two-time slices (map view) and one cross section (road cut view). In **Figures 3–9**, **11**, cross sections are rendered using data for acoustic amplitude. Time slices in **Figures 3–9**, **11**, are displayed using similarity data at 60% transparency overlying amplitude data, to allow better visualization of discontinuities. The images presented are bounded by an upper time-slice at 125 ms of two-way travel time (TWT) (∼96 m) and a lower time-slice at 350 ms TWT (∼279 m), with the cross-section point of view moving from north to south. The sections presented here capture the architecture of the fault systems and their along- and across-margin interaction. The locations of vertical profiles presented with respect to the entire data volume are labeled in **Figure 1C**.

Figure 3 presents a vertical profile at crossline 1790. The yellow dashed line shows the boundary between the crossline (1790) and the time-slice (350 ms). The other dashed lines show locations for crosslines displayed in **Figures 4–8**. We will describe the features from north to south. Several fault segments enter the survey volume from the northwest; the faults exhibit an along-margin parallel strike. These segments tend to terminate close to the surface; however, seafloor offset in most cases is not observed in the data volume. Prominent changes in slope morphology and subsurface reflector geometry are observed across the two largest fault segments (labeled i and iii, **Figure 3**). Minor surface expression is observed coincident with fault iii. A high-angle (≥80°) or vertical dip on all the segments is observed in cross section 1790. North of where fault iii exhibits a left lateral jog, a small, semi-circular anticlinal structure is observed in the crossline (1790) and the time-slice (350 ms; **Figure 3**). This structure is bounded by fault vii which exhibits curvilinear character and merges likely as a splay of the larger segment, fault iii. Continuing northeast, the limb of the anticlinal structure is imaged in the crossline and has a northeastward dip. The anticlinal structure is also imaged in the time slice by a circular acoustic reflection pattern that is bounded by fault segments iii to the west (**Figure 3**), and vii to the east. Along the outer shelf upper slope, a seaward thickening wedge is observed in the 3D P-cable cross lines and in the time-slice as a slightly deformed, folded acoustic pattern.

Moving south to crossline 1945 (**Figure 4**), the anticline is dissected by numerous fault segments (e.g., i, ii, and iii; **Figure 4**). The curvilinear nature of fault vii can be observed as the fault bounds the anticline observed in **Figure 3**. Segment vii sharply delineates stratigraphy to the north that is gently dipping seaward, from steeply dipping stratigraphy toward the fault. To the southeast of segment vii, visible in the time-slice, is a synclinal structure likely created by right-lateral pull-apart deformation as strain is distributed from fault iii to fault vii. The western edge of the syncline appears to terminate abruptly into fault iii (**Figure 4**) and the syncline forms a narrow "cuspate-like" antiform structure to both the north and the south.

Fault iii is steeply dipping in this region (**Figure 4**); the reflections imaged to the south west off fault iii exhibit a synformal geometry. Fault vii is observed north of the northern-most "cuspate-like" structure. Farther south of the horn, fault vii curves to the southwest and the stratigraphy transitions laterally from a fault (**Figure 4**) into a fold (labeled in **Figure 5**).

Between faults i and iii – both in the crosslines and time slices – there is an acoustically transparent to semi-transparent and chaotic character with only minor reflectivity. A pronounced change in acoustic reflectivity correlates with the shelf edge in this region; the increase in acoustic amplitude is bounded to the east by fault i. Along the shelf edge east of fault iii there are some concordant reflections that are flat lying in the crossline and appear to have a lower acoustic character in the time slice. Continuing to the southwest of fault iii, the antiform is dissected by numerous faults, the largest of which are labeled on **Figure 4** as faults i and ii. Reflectors exhibit increased deformation near the antiform. The wedge of acoustically transparent material along the western slope, also imaged in **Figure 3**, is likely a slump from the shelf break. The irregular nature of the western edge of the time slice reflects the intersection of the data volume with canyon heads on the outer shelf upper slope.

Crossline 1945 (**Figure 4**) is 291 m north of Crossline 2038 (**Figure 5**), but on scales of tens of meters, marked changes in the acoustic reflections imaged in the 3D data can be observed. North of the horn of the "cuspate feature," a fold is observed northeast of fault segment iii. The fold tracks the termination of fault vii. The southwest limb of the anticline to the west of fault iii is highly faulted and deformed. Farther southwest of fault segment i, amplitude reflections in the limb are steeper, but more continuous and exhibit only some minor folding. The seaward thickening wedge observed to the north is systematically increasing in thickness toward the south.

Moving southeast from crossline 2038 (**Figure 5**) to crossline line 2252 (**Figure 6**), the fold northeast of fault segment iii evolves into a monocline with abrupt increase in dip toward the west near fault iii. Note that several fault segments along the northeastern portion of the data volume bound the "cuspate" morphology. Large areas of the volume are acoustically transparent to semi-transparent with broken, chaotic reflectors. Acoustic reflectivity increases along the outer slope with mild folding near fault segment ii.

A large antiform structure is observed where fault segment vi exhibits a left lateral jog from south to north. **Figure 7** shows the marked change in acoustic reflectivity with the faulted antiform clearly imaged. Crossline 2457 intersects the time slice in a region where a circular pattern of reflectivity is imaged in the time slice northeast of fault segments v and vi. A faulted anticline, imaged in previous figures, is also well imaged in crossline 2457 (**Figure 7**). The seaward thickening lens observed in **Figure 3** thins away to the south and is not observed in **Figure 6** or **Figure 7**. Two large canyons are imaged along the seaward edge of the time slice

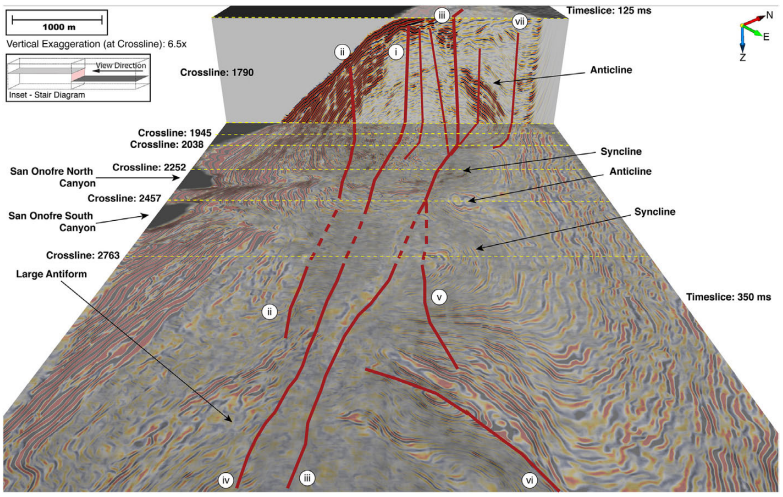

FIGURE 3 | Vertical profile of crossline 1790 amplitudes showing fault interpretations in solid red Location of the crossline, relative to the survey area, is shown in **Figure 1C**. All crosslines shown in stair diagrams are bounded by time-slices at 125 and 350 ms. Both time-slices for all stair diagrams in **Figures 3–9**, **12** are rendered using a combination of similarity data and amplitude data at 60% transparency. View direction is toward the northwest. Thick lines denote major fault segments i, ii, and iii. Thin lines denote secondary fault systems no; faults are dashed in the lower (350 ms) time-slice, where there is more uncertainty. Alternating anticline/syncline sequence can be observed in the lower time-slice. The outline of a large structural dome, labeled as a large antiform, is observed toward the bottom of the figure in the lower time-slice. Yellow dashed lines show locations of crosslines shown in other figures. Black areas in the southwest part of the lower time-slice represent shelf incisions from channelization. (Inset) Schematic view of data volume depicting view angle of stair diagrams used in this paper.

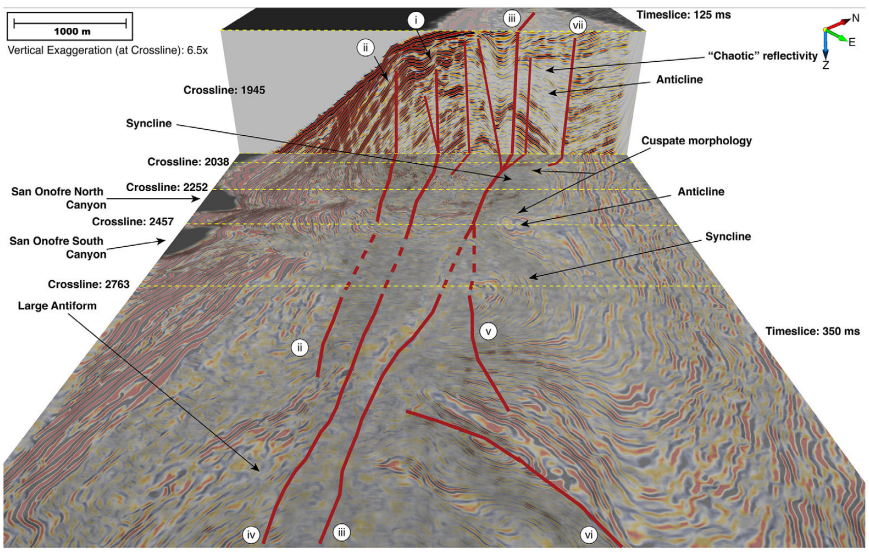

FIGURE 4 | Stair diagram of crossline 1945 with interpreted faults displayed using solid red lines. Location relative to the survey area, is shown in **Figure 1C**. Fault interpretations with more uncertainty are shown as dashed red lines in lower (350 ms) time-slice. Much of the minor faulting and deformation shown is bounded between fault segments ii and iii along the outer shelf edge. In the crossline, deformation between fault segments iii and vii is narrower than in **Figure 3**, as the plane of fault segment viii moves closer to splays of segment iii. Segment iii represents the main fault plane and is the only plane shown that extends upward past the upper (125 ms) time-slice.

as large embayments just south of the crossline. Farther south (**Figure 8**), westward dipping reflections are imaged east of fault segment iii and correlate with a circular reflection pattern in the time slice. High amplitude chaotic reflectors are imaged in the upper portions of the crossline with acoustically transparent to chaotic semi-transparent regions beneath (**Figure 8**).

Crossline 2457 (**Figure 7**) intersects the time-slice between two large canyons on the slope (**Figure 1C**). Both canyons are imaged as embayments in the time slice on **Figure 6** and labeled San Onofre Canyon North and San Onofre Canyon South (labeled "SOCN" and "SOCS," respectively, on **Figure 1**; Wei et al., 2019). An acoustically transparent region is observed

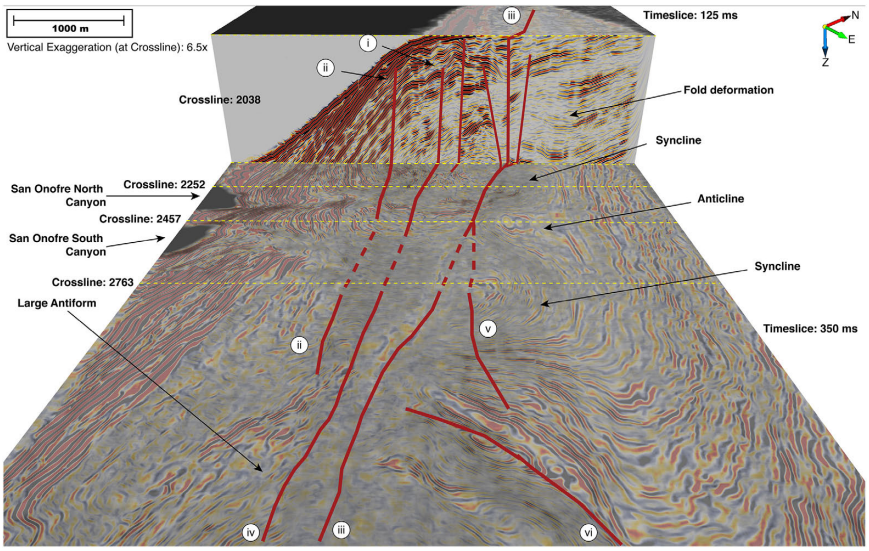

FIGURE 5 | Stair diagram of crossline 2038 with interpreted faults shown with solid red lines. Location relative to the survey area, is shown in **Figure 1C**. Faults are dashed where there is acoustic transparency, which introduces uncertainty. Fault plane of segment vii has terminated and been replaced with fold deformation. Sediment from northeast is laminar and acoustically transparent until fault segment iii. Reflector amplitude is visibly more prominent on southwestern side of segment iii.

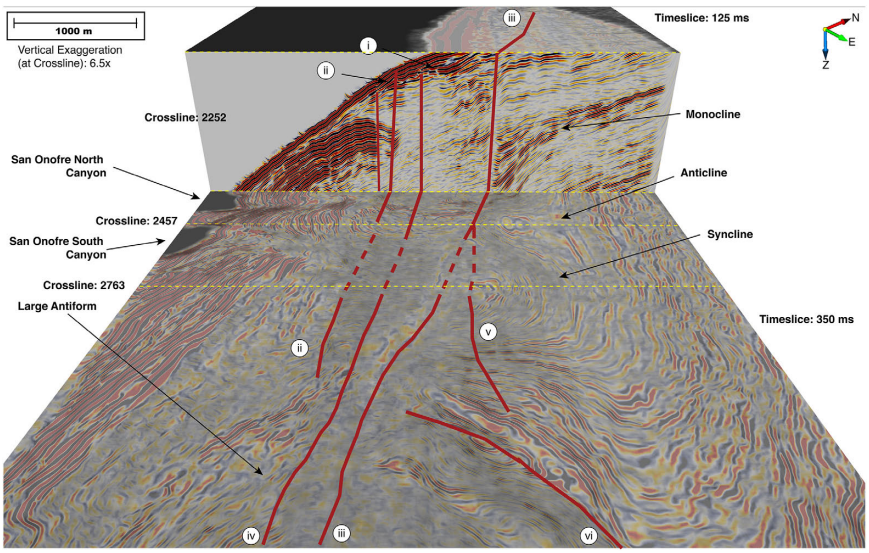

FIGURE 6 | Interpreted stair diagram of crossline 2252. Fault interpretations shown with solid red lines; dashed where interpretations have more uncertainty. Fault fold shown in **Figure 5** has been replaced by a monocline terminating at fault segment iii. Yellow dashed lines in lower (350 ms) time-slice represent locations of crosslines shown in other figures. Location relative to the survey area, is shown in **Figure 1C**.

immediately south-east of the crossline making confident interpretation difficult; however, reflector offsets in crosslines and geometry in the time slice allows for potential correlation of the fault segments between faults i and iv and that uncertainty is shown by the dashed fault trace in the region. Farther east in the volume, reflection continuity in both the crossline and the time slice allows for confident correlation of faults iii and v with fault vi (**Figure 7**). Toward the northeast in the data volume the dipping packages observed in cross section are imaged as parallel features with moderate acoustic reflectivity in the lower time slice. Between fault segments i and iii in the crossline, several fold-fault structures are imaged. Southwest of fault i, there is a more uniform dip of the slope reflections with moderate deformation. The fault geometry along fault vi exhibits a left jog just before the large anticlinal structure located at the center of the survey area (**Figure 7**). There is a dramatic change in reflection dip across

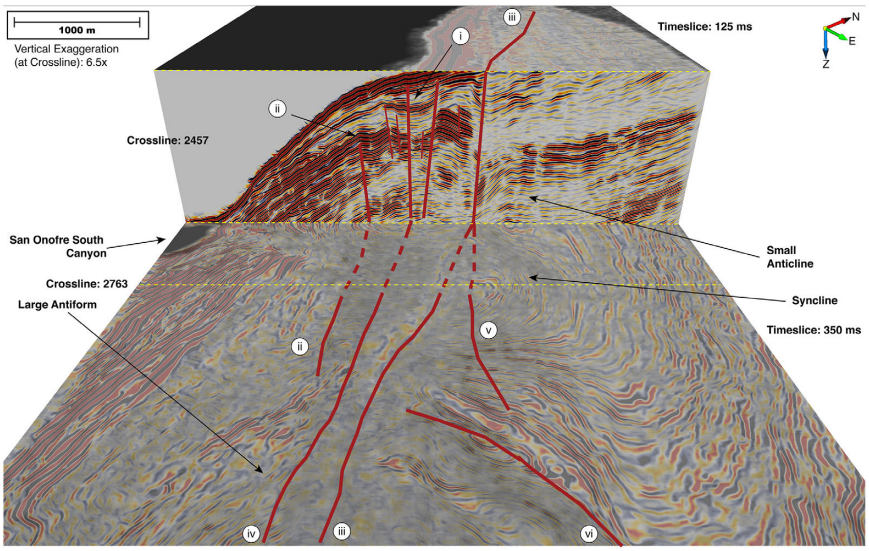

FIGURE 7 | Stair diagram of crossline 2457. Crossline is rendered in amplitudes and shows a seismic cross-section very near San Onofre South Canyon, and north of large antiform structure. Acoustic and deformation character both visibly changes on either side of fault segment iii. Yellow dashed line shows location of crossline 2763.

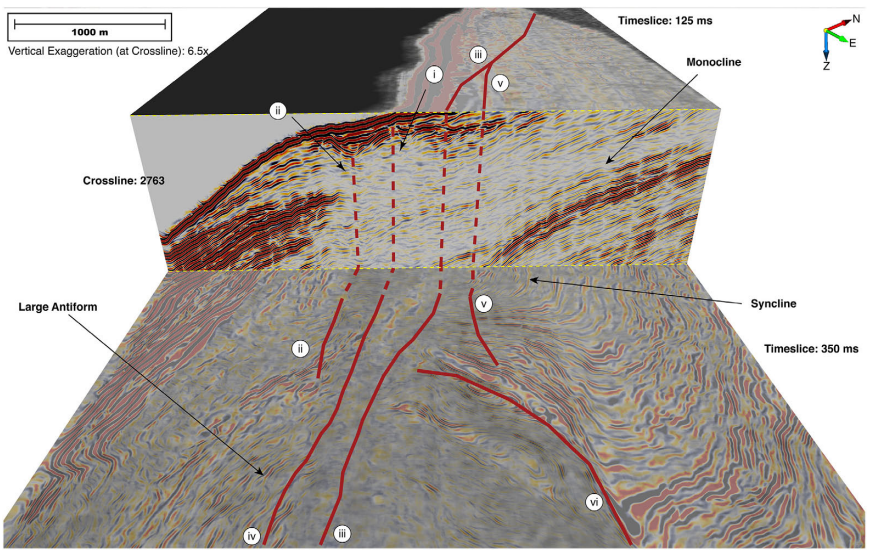

FIGURE 8 | Interpreted stair diagram of crossline 2763 using amplitude data for the crossline and bounded by time-slices at 125 and 350 ms rendered using similarity seismic attribute. Stratigraphy is acoustically transparent in the center of the crossline, possibly due to fluid presence or fault damage from large fault segments in crossline. Fault interpretations are shown with solid red lines; dashed where there is more uncertainty. A monocline to the north exhibits sloped stratigraphy to the south. Stratigraphy along shelf edge maintains a shallower dip and stronger reflections at depth.

the margin; toward the northeast the stratigraphy is acoustically laminated with a shallow dip, whereas toward the southwest of fault segment ii the dip of the stratigraphy appears to steepen. On the outer shelf, the westward dip of the upper slope reflections diminishes where the width of the shelf increases.

Fault fold deformation farther to the southeast is observed in crossline 3400 (**Figure 9**). In this region where the shelf is wider, no canyon morphology is observed along the seaward side of the data volume. Fault deformation is very pronounced and focused across a few major fault segments. Crossline 3400 images the eastern limb of a large anticlinal structure near the center of the data volume (**Figure 1C**). The anticlinal structure measures roughly 2500 m in diameter and is an E-W elongated structural dome imaged in the lower time slice (**Figure 13**). Two large fault segments, iii and iv, bisect the antiform in the crossline separating the northeast and southwest limbs. Fault iv appears

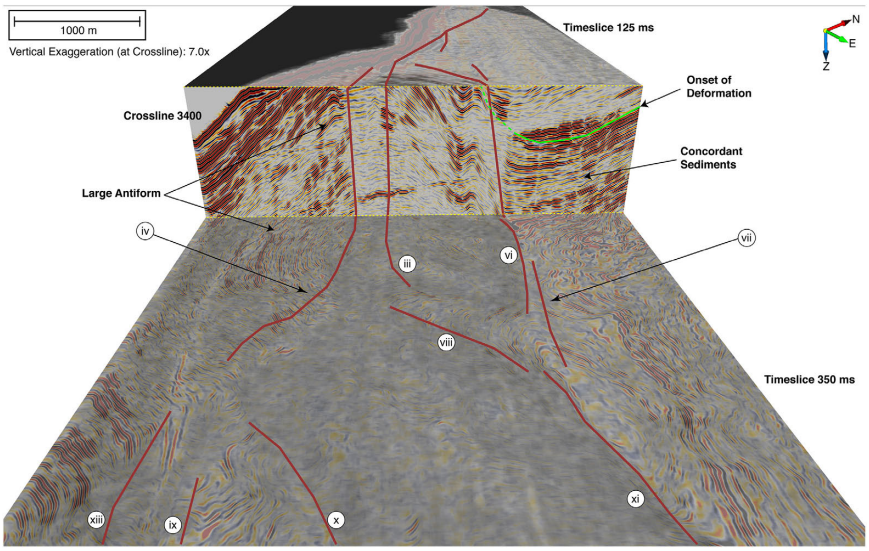

FIGURE 9 | Interpreted stair diagram of Crossline 3400 bounded by time-slices at 125 and 350 ms. Time-slices are displayed as a combination of similarity data and amplitude data at 60% transparency. Major fault segments are labeled. This crossline cuts through the middle of the large anticline structure observed in Zone Two of the survey area. Lower time-slice shows fault segments delineating an acoustically transparent to semi-transparent region in the middle of the time-slice. Note some of the faults exhibit a more northwesterly trend in this region. Solid green line delineates stratigraphic horizon recording the onset of deformation (lowest depth is 200 ms or ∼156 m). Dashed green line shown where horizon is inferred. Locations of seismic lines are shown in **Figure 1C**.

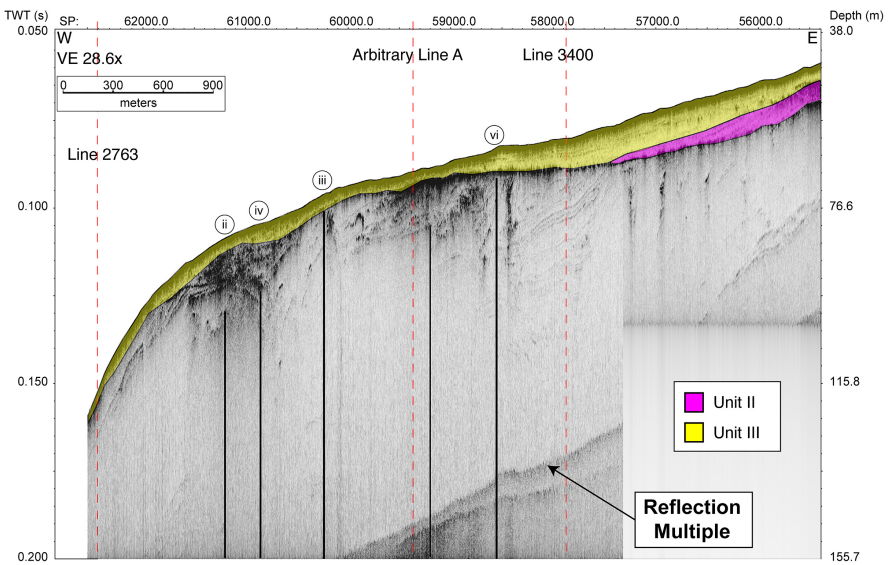

FIGURE 10 | CHIRP seismic profile from 50 to 200 ms (∼38–156 m) depth. Red dashed vertical lines show locations of other crosslines and arbitrary line. Major faults shown in black are labeled. Mapped units II and III are correlated to interpretations published by Klotsko et al. (2015). Multiple is labeled.

to exhibit a surface expression (**Figures 4**, **5**: Sahakian et al., 2017).

Between the cities of Newport and San Diego the continental shelf is relatively narrow, averaging 2.5 km in width (**Figure 1B**). The shelf offshore of San Onofre is anomalously wide however, extending to approximately 10 km. The location of the large antiform structure observed in the lower time slice (**Figures 3**–**9**) is spatially coincident with this widest part of the shelf (see crossline locations in **Figure 1C**). Stratigraphy to the northeast of the anticline crest, is bounded by the vi segment; the reversal of dip in this region separates the northeast limb of the anticline from the more gently southwest dipping nearshore reflectors. Toward the southwest of the anticline axis, the reflections are steeply dipping with minor faulted stratigraphy in crossline 3400.

Reflectors in both limbs of the anticline are clearly truncated at the seafloor, likely from transgression of sea level across the

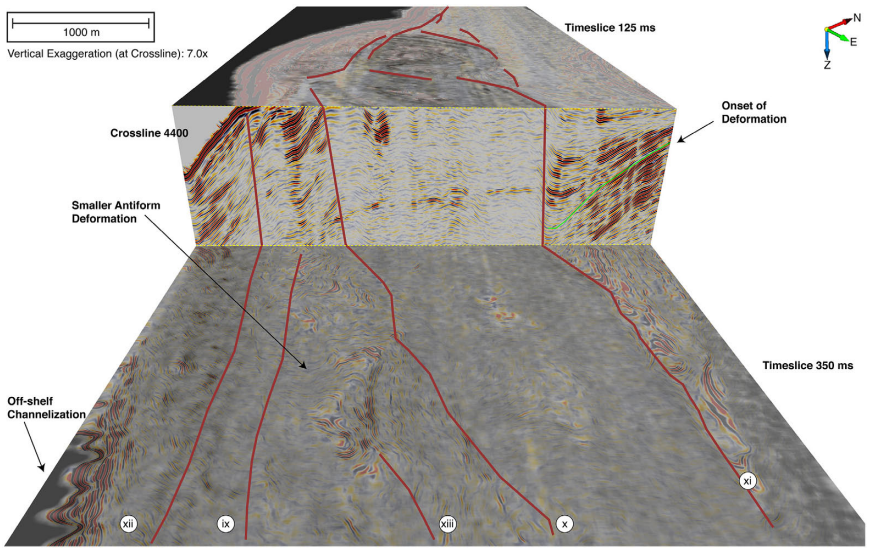

FIGURE 11 | Interpreted stair diagram of Crossline 4400 with major fault segments labeled. Crossline is bounded by time-slices at 125 and 350 ms (~96 and ~279 m), rendered using similarity data combined with amplitude data at 60% transparency. A smaller anticline is observed in the lower (350 ms) time-slice west of fault segment x. Note the monocline in the crossline north of fault segment xi. Green line traces stratigraphic horizon that records onset of deformation. Locations of seismic lines are shown in **Figure 1C**.

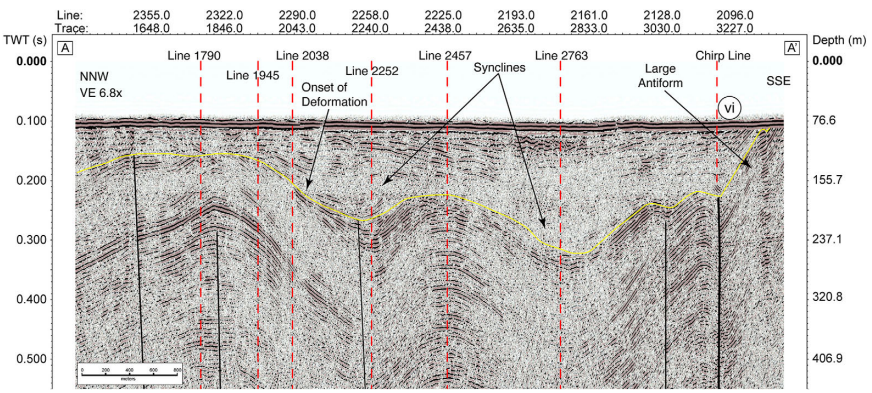

FIGURE 12 | Interpreted arbitrary line across northern section of survey are from A to A'. Location of seismic line is shown in **Figure 1C**. Minor faults are shown with thin black lines. Major faults are shown with thick black lines and labeled. The view is to the northeast, toward the coastline. Reflector color has been desaturated for ease of interpretation. Red dashed lines trace locations of crosslines shown in previous figures. A sequence of anticlines and synclines is imaged across the arbitrary line, terminating at the northern limb of the large mid-shelf antiform structure (labeled).

continental shelf. A marked change in dip occurs northeast of the anticline at 200 ms (~156 m) and is outlined with a yellow line in both **Figure 9**. Younger stratigraphy near fault segment vi is undeformed above the line, and thus we infer this boundary to be the onset of fault deformation from vi. In **Figure 9**, the line is dashed to show the inferred boundary where the data is acoustically transparent.

Figure 10 shows an east-west line of CHIRP data acquired by Scripps Institution of Oceanography (SIO) in 2008 using a customized EdgeTech X-Star CHIRP sub-bottom reflection sonar with sub-meter vertical resolution. Data were heave-corrected and processed to 200 ms TWT. The line was selected because it passes through the northern limb of the large anticline at the widest part of the shelf and intersects several of the larger fault segments. Due to masking of surficial stratal geometry by oscillations from the bubble effect in the 3D data, this line was selected to investigate any near-surface fault offset. We extended and labeled our fault interpretations into the CHIRP line shown in **Figure 10** and correlated interpreted sediment horizons with units described by Klotsko et al. (2015). Unit III is an acoustically transparent layer that could be mapped across the entire line and represents a modern marine deposition layer (Klotsko et al., 2015). None of the interpreted fault segments could be mapped into Unit III although the boundary between underlying stratigraphy and Unit III, the transgressive surface, exhibits considerable offset.

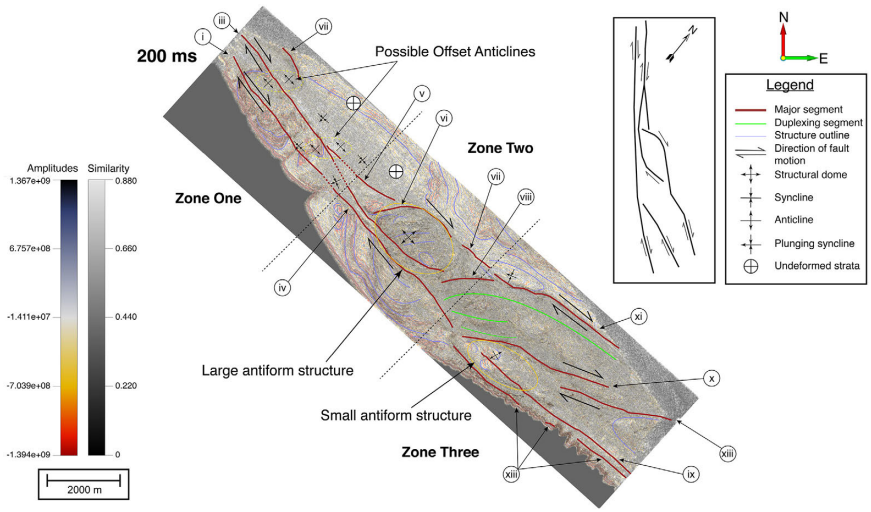

FIGURE 13 | Map view of time-slice 200 ms (~156 m) showing major fault interpretations and right-lateral movement. Time-slice is a combination of amplitude data, overlapped with similarity attribute data at 60% transparency. The survey area is divided into three zones based on fault character and acoustic facies. Solid yellow ovals outline area of large and small anticlines in Zones Two and Three. In Zone One an alternating sequence of anticlines and synclines is imaged. Dashed yellow ovals group possible offset anticlines. Green lines denote possible duplex faulting. Light purple lines outline structures and patterns in the amplitude data. Inset shows a simplified kinematic diagram of the major faults in the survey area.

Farther southeast of the anticlinal structure, the observed major fault segments outline a large area that is acoustically transparent and approximately 3 km wide. The major fault segments can be divided into two groups based on their strike: fault segments that are parallel to the shelf edge and bisect the anticline (e.g., fault segments iii and iv); vs. fault segments that exhibit a more northwest to southeast trend (**Figure 11**). In this region, the fault segments have steep dips, being almost vertical. In **Figure 11**, fault segment xi appears to be the largest segment bounding the acoustically transparent zone to the southwest. Stratigraphy inshore of this fault is acoustically laminated with a dip toward the southwest down to approximately 150 ms, with moderate acoustic reflectivity and is observed in the lower time-slice. The dip of this package appears to increase markedly with depth.

Fault segment x is the southwestern bounding fault of the acoustic transparent zone (**Figure 11**). Between this fault and the shelf edge, the reflectors tend to parallel the slope with a steep dip. Within these bounding fault segments, there are numerous smaller segments and several zones of deformation associated with these smaller segments. Between the fault segments xii and x, the reflector character is acoustically transparent to acoustically semi-transparent and chaotic with minimal reflector continuity. Southwest of fault segment x, there is higher acoustic reflectivity and reflector continuity. Along the western edge of fault segment x in the middle of the time-slice where the fault jogs to the west there appears to be a small anticlinal structure (**Figure 11**).

Near the southeastern limit of the survey area the shelf width again diminishes and small canyon embayments are observed in the time slice. Canyons in this location exhibits a maximum slope of 24° on the continental shelf (**Figure 14**). Examination of the 3D volume in this region reveals a highly chaotic acoustic character being mostly acoustically transparent to semitransparent; as such there is much uncertainty in fault location in this region. Our fault interpretations delineate areas with markedly different acoustic character. Where mapped, the fault segments in this location exhibit a predominantly NW-SE trend.

Figure 12 shows a vertical display of amplitude data from 0 to 800 ms of an arbitrary line (marked A to A' in **Figure 1C**). This line images a sequence of synclines and anticlines from north-northwest to south-southeast. The axes of all the imaged folds is northeast-southwest. The northern limb of the large anticline coincident with the widest part of the shelf is imaged to the far south-southeast and displays steeply dipping stratigraphic bedding. In this location, as in **Figure 9**, bedding terminates at the seafloor. The largest syncline imaged in the arbitrary line, centered around trace 2800, appears to plunge seaward with a west-southwest axis and is coincident with the San Onofre South (SOS) off-shelf drainage channel (Wei et al., 2019). A smaller syncline to the north, centered at trace 2240, also appears to plunge seaward, toward the San Onofre North (SON) drainage channel (Wei et al., 2019). Separating the two synclines is an asymmetric anticline, measuring 1686 m across at the arbitrary line in **Figure 12**, and narrowing to 1040 m near the shelf edge. Finally, an anticline exhibiting a tight fold, is found to the north centered around trace 1800 suggesting a northwest vergence. This anticline terminates abruptly against fault segment iii. The western limb of the anticline is possibly shifted northwards approximately 252 m along the western side of the fault (northern dashed yellow oval in **Figure 13**). A second possible offset of approximately 116 m is observed along the same fault (fault segment iii) on the next anticline to the south (southern dashed yellow oval in **Figure 13**).

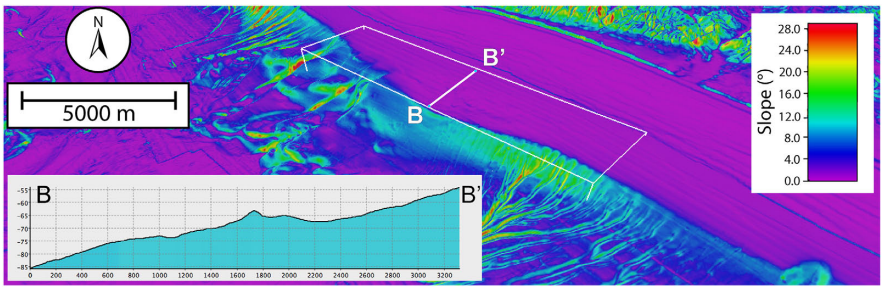

FIGURE 14 | Oblique view of continental shelf and slope bathymetry off the coast of San Onofre and San Clemente, showing location of survey in white 3D box. Colors denote slope angle. Inset shows slope along an arbitrary cross-section from B to B' passing through large antiform coincident with widest part of the shelf.

A survey-wide analysis of our interpreted faults reveals two major azimuthal trends of the faults in the study region. Based on these trends and acoustic reflectivity, we divided the study area into three zones, labeled in **Figure 13**.

Fault azimuths in Zone One are oriented roughly toward the northwest. The largest fault segment, iii, bounds an undulating series of smaller synclines and anticlines (shown in cross-section in **Figure 12**). Segment iii delimits Zone One between undeformed sediments trapped from the east and deformed dipping stratigraphy seaward.

Zone Two is dominated by a large structural dome coincident with the widest part of the continental shelf. This antiform structure is bisected by the largest segments (fault segments iii and iv) in the survey area and is bounded on the eastern edge by fault segments vi and vii. As in Zone One, sediments from the east gently dip toward easternmost boundary faults. These boundary faults exhibit a left-ward jog and change trend to a more northwest azimuth as they approach Zone One. Segments iii and iv also exhibit small changes in azimuth to the northwest in the northern part of Zone Two.

In the south (Zone Three), the largest difference in fault azimuth and acoustic character is observed. A marked change in fault trend of 25° occurs between Zones Two and Three, and 32° between Zones One and Three. Fault segments in Zone Three have a more NW-SE trend and a small anticline is observed where fault segment x exhibit a small change in trend toward the northwest and interacts with segments ix and xii. As opposed to Zones One and Two, much of Zone Three is acoustically transparent and difficult to interpret except at boundaries where there are large amplitude differences.

Truncated stratigraphy of the large anticline in Zone Two forms an angular unconformity near the seafloor; however, subsurface deformation has a surface expression as shown in a map of bathymetry data (**Figure 14**, line B to B'). The inset shows a transect across the anticline with approximately 5–7 m of surficial relief across the large regional anticline observed in Zone Two (**Figure 13**). Note the small increase in slope along the shelf edge near B on the transect and along the shelf edge to the south of the widest part of the shelf. As expected, the continental shelf and basin floor in this region have low slopes with localized steep slopes coincident with off-shelf channelization. The steepest slopes in the survey area are located above the basin floor at the toe of the slope and are up to 25°. The large canyons in the northern portion of the study region (SON and SOS) incise the shelf edge (**Figure 14**; Wei et al., 2019).

Paleochannel Identification

In the ICB coastal margin, about half of the regional offshore canyons and most of the smaller gullies appear to be active during the Last Glacial Maximum but were rendered inactive when cut off from canyon heads on the outer shelf during post-glacial transgression (Normark et al., 2009). These bathymetric features make ideal candidates for fault piercing points to measure offset and estimate slip-rate.

Piercing point candidate gullies and canyons on the shelf and slope were identified in time-slices. Several slope features were found to be potentially offset by shore-oblique faults that are likely part of the San Onofre Trend, but there was no observable offset from NIRC segments found in gullies on the shelf. Attempts at mapping channel thalweg horizons below the seismic signature to determine piercing points were inconclusive due to the presence of chaotic amplitude reflectors in the data.

DISCUSSION

3D Structure Mapping

Acquiring 3D seismic reflection data is critical to image fault segment interactions especially along steeply dipping strike slip fault systems, such as NIRC. Such a data volume places important constraints on how deformation is communicated to neighboring fault segments, permitting or arresting through-going rupture. Fault analysis in three-dimensions has allowed us to capture the architecture of the NIRC fault segments throughout the survey area and illustrate their curvilinear character (**Figure 13**). Our observations are that distribution and architecture of the fault segments changes throughout the volume. This distribution has implications for rupture behavior and propagation, as well as direct controls on margin architecture such as shelf width, drainage patterns, and tectonic structures. These changes in architecture have allowed us to further assign three separate zones of deformation imaged in the survey area.

Zone One encompasses mapped segments of the Camp Pendleton splay in the northwestern section of the survey

and the zone is bounded to the south by a large antiform structure (**Figure 9**). In this zone, we observe a transition from a transtensional to transpressional regime accompanying these segments. Ryan et al. (2009), with an industry MCS line only two kilometers north of crossline 1790 shows that transpressional features predominate northward along the Camp Pendleton splay, and eventually disturb the seafloor near Dana Point (Ryan et al., 2009). We attribute this change in strain regime to a series of right and left jogs in fault segments that are expressed in the deformation as a series of synclines and anticlines bounded by the main fault segment, segment iii (**Figure 1C**). Given the 3.125 m bin size of the data volume in all directions, the terminations and transitions of these faults into folds and then eventually monoclines, are well-imaged in the data (**Figures 3**–**6**). These transitions are associated with secondary fault splays and step-overs that creates a "cuspate-style" morphology in the time slice acoustic reflectivity, with the horns of the cusp being antiforms and intervening regions of the cusp being synforms (**Figures 5**, **6**). Two major strands of the NIRC fault (iii and v) bound these semi-circular patterns of acoustic reflectivity in the time slice to the southwest (**Figure 4**).

We observe the completion of the transition to transtension in crossline 2457 (**Figure 7**). The faulting and folding of the anticline along the outer shelf exhibit a keystone structure with a negative flower structure, as evidence for transtension in this region. At this location, the damage zone of the fault plane is fairly wide, in contrast to the narrow fault zone of the inshore fault.

The internal structure of the anticline is no longer well-imaged as the point of view moves northwest into the data volume to crossline 2252 (**Figure 6**). Here the anticline exhibits a transparent alternating to semi-transparent acoustic character. We interpret that this loss of acoustic reflectivity may record intense shearing and deformation or possibly fluid flow in the region, which has overprinted the existing acoustic impedance contrasts. Farther north at crossline 2038 (**Figure 5**) and crossline 1945 (**Figure 4**), the acoustic reflectivity of the anticline returns, and the internal deformation is observed with a transtensional, down-dropped geometry.

At crossline 1790 (**Figure 3**), the shelf begins to narrow in this area and the acoustic character has reverted back to transparent and semi-transparent but chaotic. Such changes along the margin are more likely resulting from shearing and overprinting the acoustic character than lateral facies changes with different acoustic impedance contrasts. Our preferred interpretation is the along margin change in acoustic reflectivity is the result of post-depositional processes (i.e., shearing or fluid flow).

An azimuthal change of 15° is observed when moving from the northern zone (Zone One) to the central zone (Zone Two; **Figure 9**). Two segments form a keystone structure from the surface to about 200 ms (∼156 m) in depth that bisects the large antiform. Sahakian et al. (2017) identifies this keystone structure as concomitant with the location of a possible drainage channel.

The faults observed in Zone Three exhibit both fault trends and the changes in those trends results in an anticline along the northwestern margin of Zone Three (**Figures 6**, **9**). A wide zone of acoustically transparent to semi-transparent chaotic character exists in Zone Three and we interpret this acoustic character to record a wide zone of shearing bounded by large faults that strike NW-SE. Problems with acoustic reflectivity persist throughout Zone Three and make interpretation difficult. These problems have been documented previously by Ryan et al. (2009) who found intermittent areas acoustically "wiped out" downward from the seafloor, just south of our survey area between Las Pulgas Road and Oceanside.

Toward the north these fault segments converge and left step into the large antiform structure coincident with the widest part of the shelf and near the center of the survey. The boundary between observed acoustic reflectors and transparent to semi-transparent character are interpreted to be shear zones at segment locations. These shear zones probably represent the step-over between more northwestwardly striking segments on the eastern edge of the data volume and the coast-parallel segments on the western edge of the data volume. It is possible that strain in this location is being partitioned through duplexing structures (light green segments in **Figure 13**). These structures are the end of segments that change strike from northwest to more northerly. Strain appears to be transferred to several large segments in the step-over that, in turn, then crosscut the large antiform structure.

Leftward steps on a right-lateral system result in localized compression and frequently form deformational structures such as pressure ridges (or "pop-up structures"). There are three other documented left-ward jogs on NIRC, each resulting in pressure ridge structures. The Torrey Pines strand interacts with the Carlsbad Canyon strand just to the north of Carlsbad Canyon and creates a northwest trending ridge that extends for 15 km (Ryan et al., 2009). Another pop-up structure occurs from a jog between the Torrey Pines strand and the La Jolla strand offshore of Torrey Pines State Reserve (white triangles in **Figure 1B**; Hogarth et al., 2007; Le Dantec et al., 2010). Finally, onshore segments of the Rose Canyon Fault left jog to the offshore La Jolla strand near the neighborhood of La Jolla in northern San Diego and create Mount Soledad, with approximately 150 m of uplift (Hogarth et al., 2007). The large antiform in Zone Two is in the shape of a structural dome, roughly egg-shaped, and approximately 2 km wide at the deepest point in the data volume. The structure is transpressional and coincident with left-stepping right-lateral segments between the Carlsbad Canyon strand and Camp Pendleton splay (Sahakian et al., 2017).

Strike-slip fault planes often transition into extensional fractures before terminating (Corbett et al., 1991) and despite the overall transpressional regime controlling the uplift of this antiform, two large fault segments bisect the middle of the antiform and display evidence of transtension including a negative flower structure also previously documented by Sahakian et al. (2017). Fault architecture provides further evidence of transtension at the antiform. The terminating segment of fault iii from the northwest and fault vi from the southeast tend to curve around the eastern half of the antiform feature in a hook pattern. The pattern is similar to en-passant linkages observed at scale in loaded granite microcracks (Kranz, 1979). En-passant linkages occur when the stress field at the tip of a propagating fracture deflects the tip of an approaching fracture away from it. Both tips deflect around each other until each is removed from the influence of the other's stress field. Then

the tips curve toward the opposite fracture and connect (Kranz, 1979; Corbett et al., 1991). En-passant fracture linkages tend to be associated with extension or transtension (Corbett et al., 1991).

The antiform creates a local bathymetric high in the area, which can be observed in profile in **Figure 14**. The relief on the seafloor in this region exhibits a 5-meter difference as shown between points B and B' in the profile. In fact, east of the bathymetric high, the seafloor dips slightly landwards toward the margin. The uplift and consequent bathymetric relief acts to divert offshore drainage flow to the north and south, around the main portion of the antiform structure. The bathymetry data show a lack of canyons and gullies on the slope to the west of the observed antiform (**Figure 14**). A lack of sedimentation due to diversion of drainage is further supported by a shallow gravity core from the slope (BB 13–14; location shown in **Figure 1C**). We discovered that this core contained radiocarbon dead sediments at only 40 cm depth.

The relatively undeformed reflectors with lower acoustic reflectivity observed to the east are recording sediments trapped against the eastern limb of the anticline (**Figure 9**). Given the thickness of the sediment overlying the highly deformed and faulted reflections together with extrapolated sediment rates yields the onset of more recent faulting along this segment of the NIRC to be 560,000 to 575,000 years before present. Unfortunately, a great deal of uncertainty into the extrapolated sedimentation rates as well as age of onset of faulting is due to the shallow penetration of our cores.

The sediment transport deflected to the north by the anticline is captured by two large drainage channels northwest of the antiform structure that incises the shelf edge (in Zone One). The main fault segment continues northwestward along the margin; however, several smaller fault segments appear to control these channels with right-lateral offset visible at the surface. A dendritic-shaped network of small channels accommodates flow diverted to the south by the large anticlinal structure. Typical dips of the seafloor along continental slopes are approximately 4–6°; however, at the location of the channels south of the anticline exhibits slopes along the shelf/slope break of 12–21°. This scarp is aligned with several fault segments striking parallel to the margin. The greatest slopes are observed at the toe of the slope (∼25°) and are interpreted to be pop-up structures associated with left steps along right lateral fault segments.

Sahakian et al. (2017) noted that the NIRC segments in the vicinity of SONGS showed no displacement of the transgressive surface, consistent with our observations. Despite deformation recorded at the seafloor in the survey area, CHIRP data acquired over the large antiform at the widest part of the shelf shows large fault segments terminate very close to the transgressive surface, but no displacement of modern marine sediments were imaged (**Figure 10**).

In the acoustic amplitude data, paleochannel thalwegs were difficult to confidently identify; however, the uncertainty was reduced when the data were rendered using most negative and most positive curvature seismic attributes (see **Supplementary Figure 3**). By coblending the two attributes paleochannels are enhanced in the time-slice view. Using these attributes, gullies extending to the base of the slope can be imaged down to 545 ms (∼446 m), and traces of the largest off-shelf drainage channels are imaged in Zone One at depths down to 440 ms (∼355 m). Reflectors tended to become chaotic with depth due to fault shear and possible fluid flow, so candidate paleochannels on the shelf could only be confidently imaged to a shallow depth, approximately 160 ms (∼124 m). Chaotic reflections also made mapping of shelf thalwegs impractical and thus we were unable to confidently locate offset across mapped fault segments.

Seismicity and Through-Going Rupture

No large earthquakes have been recorded on any segment mapped in the survey area in the recent past; epicenters recorded since the 1930s for earthquakes greater than a M3.0 show a lack of recent activity along the San Onofre portion of the NIRC system (**Figure 1B**) and a general gap in recent major seismicity along the entire fault system southwards into San Diego (Anderson et al., 1989). The area has experienced only low rates of microquake (M1.0–2.0) activity in recent times (Grant and Shearer, 2004). Large earthquakes, however, have been recorded near the fault system's endpoints. The most recent event is the M6.4 1933 Long Beach Earthquake, epicentered on the northern end of the system. At the time of that rupture, epicenters were not precisely known, and had to be calculated by hand based on seismogram and shake reports from the area (Hauksson and Gross, 1991). The most likely epicenter for the mainshock has been on a segment offshore of the city of Newport Beach. Conversely, in the southern onshore segments there have been no large seismic events on main segments of the system since the founding of Mission San Diego in 1769 but trenching surveys in San Diego show a surface rupture, dated at AD 1650 ± 120 years, which caused 2–3 m of slip (Lindvall and Rockwell, 1995; Rockwell, 2010).

Magnitude tends to scale with fault length and recent modeling of an end-to-end rupture of the offshore segments from La Jolla cove to Newport Beach system could potentially generate a M7.3 earthquake (Wells and Coppersmith, 1994; Sahakian et al., 2017). In the 3D volume, mapped step-over widths between fault segments are mostly equal to or less than 1 km. Wesnousky (2006) observed that there was a high likelihood of through-going rupture between fault segments when step-over distances were 3 km or less (Wesnousky, 2006; Biasi and Wesnousky, 2016). This suggests that all the segments mapped in our survey area, along with segments from north of Carlsbad Canyon (south of the survey area) and onshore segments north of the survey area, could rupture together in a single event (Singleton et al., 2019). The largest step-over in the survey area is associated with the large anticline observed in Zone Two. This structure would likely not inhibit through-going rupture based on step-over width alone.

CONCLUSION

High-resolution 3D P-Cable seismic reflection data provide unprecedented imaging of fault segments off the coast of San Onofre, California. Such imagery demonstrates the importance of small step-overs and secondary fault splays in how deformation is communicated to neighboring faults. Understanding fault-fold deformation by peeling back a combination of crosslines, inlines,

and arbitrary lines for a given time slice, as well as observing sequences of time slices and horizons provides for a true 3D examination of deformation features. One of our objectives was to learn more about fault interactions at step-overs on this portion of the shelf. We were able to accomplish this objective by imaging interactions between individual segments of the NIRC at the scale of deformation, and additionally revealed the curvilinear character of many of the fault segments on this system. Another of our objectives was to image offset channels in the 3D data, however poor acoustic reflectivity in some areas and a lack of long core data introduced much uncertainty in mapping. Despite the uncertainty, we were able to confirm the presence of a large anticline at the widest part of the continental shelf due to a major leftward step-over of the main fault system.

Based on fault orientation and acoustic reflectivity, the data volume has been divided into three zones, with the northerly most two zones having more continuous reflectivity. Zone Three to the south is characterized by transparent to chaotic semi-transparent acoustic reflectivity. In Zone Two, the faults are oriented in a more northwest azimuth engendering transpression and the consequent anticline.

Zone One illustrates the marked variability in acoustic reflectivity that appears to be post-depositional in nature and is associated with intense shear deformation and/or fluid flow. Along the eastern portion of Zone One, the data volume images the transition from a monocline, into a fold, and finally into a fault in response to small changes in fault orientation and secondary fault splays. The consequent deformation created a "cuspate" geometry in the acoustic reflectivity patterns in the time slice with the "horns" being anticlines.

The large anticline observed in Zone Two traps sediments to the east, which creates a 10 km wide shelf in this region. The anticline has bathymetric expression diverting drainage to the north and south. Fault-controlled canyons that incise the shelf edge capture the northward-deflected flow. Thickness of trapped sediments to the east of the anticline suggests that the deformation of the NIRC fault system in region began 560,000 to 575,000 years before present. Age estimates from shallow penetration core data were used to extrapolate sedimentation rates, which introduced uncertainty in age estimates for the onset of deformation in this region. Future well sampling and/or longer cores are necessary to properly constrain the age and magnitude of deformation in the region.

Finally, the main strands of the NIRC fault system bound a large acoustically transparent region in Zone Three. This transparent region appears to be bounded by large fault segments suggesting the transparent region may be caused by complex shear zone. Several duplex structures are observed partitioning strain and causing compression with resulting pressure ridges.

DATA AVAILABILITY STATEMENT

The datasets presented in this study can be found in online repositories. The names of the repository/repositories and accession number(s) can be found in the article/ **Supplementary Material**.

AUTHOR CONTRIBUTIONS

JH wrote the manuscript, developed the model, and created the figures. ND and GK provided valuable guidance, extensive edits, and financed the project. All authors contributed to the article and approved the submitted version.

FUNDING

Funding for this research was provided by a grant from Southern California Edison funded through the California Public Utility Commission (CPUC), and the Maxwell J. Fenmore Memorial Fellowship. Figures were generated using Generic Mapping Tools, version 5 (Wessel et al., 2013), Kingdom Suite 2018 (IHS Markit), OpendTect (dGB Earth Sciences), and Fledermaus (QPS B.V.). Cruise information for NH1320 (2D MCS; doi: 10.7284/902996), NH1323 (3D P-Cable MCS; doi: 10.7284/903024), and TN336 (Coring; doi: 10.7284/906644) are accessible via the Rolling Deck to Repository (R2R) web interface. Seismic data are archived with Marine Geoscience Data System repository.

ACKNOWLEDGMENTS

The authors wish to acknowledge the assistance of Mike Barth of Subseas Systems, the sailing and science crews of the R/V New Horizon (NH1320 and NH1323) and R/V Thomas G. Thompson (TN336), Geotrace Technologies, and NCS Subsea, Inc., for their roles in data acquisition and processing. Our thanks in particular to Hector Perea and a reviewers who provided valuable input on enhancing and clarifying an early version of the manuscript. We would also like to thank Emily Wei for her assistance in core processing and analysis.

SUPPLEMENTARY MATERIAL

The Supplementary Material for this article can be found online at: https://www.frontiersin.org/articles/10.3389/feart.2021.653672/full#supplementary-material

Supplementary Figure 1 | Amplitude vs. Frequency graph for the triple-plate boomer seismic source used on NH1320 and NH1323. Peak frequency is 175 Hz, resulting in a minimum vertical resolution of 2.1 m.

Supplementary Figure 2 | (A) Crossline 3200 shown after industry processing but before noise removal. **(B)** Vertical profile showing combined original seismic amplitudes and dip component at crossline 3200. Dip in all directions was used as a steering parameter of the filter. Note that dip was automatically computed on low amplitude artifacts above the seafloor. These artifacts are due to ringing from the post-migration dip filtering process. **(C)** Profile of noise removed from crossline 3200 after applying a dip-steered median filter. Filter parameters were adjusted to minimize the amount of primary energy removed. **(D)** Crossline 3200 after application of filter. More continuous reflections are now observed.

Supplementary Figure 3 | Detail map view of Zone One using an interpreted time-slice at 285 ms (~225 m). Fault segment interpretations are shown as solid black lines. North is toward the top of the Figure. Time-slice is rendered using coblended Most Negative and Most Positive Curvature seismic attributes to enhance paleochannel identification.

REFERENCES

Anderson, J. G., Rockwell, T. K., and Agnew, D. C. (1989). Past and possible future earthquakes of significance to the San Diego region. *Earthquake Spectra* 5, 299–335. doi: 10.1193/1.1585524

Bahorich, M., and Farmer, S. (1995). 3-D seismic discontinuity for faults and stratigraphic features: the coherence cube. *Leading Edge* 14, 1053–1058. doi: 10.1190/1.1437077

Barrows, A. G. (1974). *A review of the Geology and Earthquake History of the Newport-Inglewood Structural Zone, Southern California*. San Diego, CA: California Division of Mines and Geology.

Bennett, R. A., Rodi, W., and Reilinger, R. E. (1996). Global Positioning System constraints on fault slip rates in southern California and northern Baja, Mexico. *J. Geophys. Res. Solid Earth* 101, 21943–21960. doi: 10.1029/96JB02488

Biasi, G. P., and Wesnousky, S. G. (2016). Steps and gaps in ground ruptures: empirical bounds on rupture propagation. *Bull. Seismol. Soc. Am.* 106, 1110–1124. doi: 10.1785/0120150175

Blaauw, M., and Christen, J. A. (2011). Flexible paleoclimate age-depth models using an autoregressive gamma process. *Bayesian Anal.* 6, 457–474. doi: 10.1214/11-BA618

Bohannon, R. G., and Geist, E. (1998). Upper crustal structure and Neogene tectonic development of the California continental borderland. *Geol. Soc. Am. Bull.* 110, 779–800. doi: 10.1130/0016-7606(1998)110<0779:ucsant>2.3.co;2

Bohannon, R. G., and Parsons, T. (1995). Tectonic implications of post–30 Ma Pacific and North American relative plate motions. *Geol. Soc. Am. Bull.* 107, 937–959. doi: 10.1130/0016-7606(1995)107<0937:tiopmp>2.3.co;2

Brookshire, B. N., Lippus, C., Parish, A., Mattox, B., and Burks, A. (2016). Dense arrays of short streamers for ultrahigh-resolution 3D seismic imaging. *Leading Edge* 35, 594–599. doi: 10.1190/tle35070594.1

Clark, K. J., Nissen, E. K., Howarth, J. D., Hamling, I. J., Mountjoy, J. J., Ries, W. F., et al. (2017). Highly variable coastal deformation in the 2016 MW7.8 Kaikôura earthquake reflects rupture complexity along a transpressional plate boundary. *Earth Planet. Sci. Lett.* 474, 334–344. doi: 10.1016/j.epsl.2017.06.048

Conrad, J. E., Brothers, D. S., Maier, K. L., Ryan, H. F., Dartnell, P., and Sliter, R. W. (2018). Right-lateral fault motion along the slope-basin transition, Gulf of Santa Catalina, southern California. *Mountains Abyss* 110, 110–117. doi: 10.2110/sepmsp.110.07

Corbett, K. P., Friedman, M., Wiltschko, D. V., and Hung, J. H. (1991). Controls on fracture development, spacing, and geometry in the Austin chalk formation, Central Texas: considerations for exploration and production. *Dallas Geol. Soc. Field Trip* 4, 1–49.

Covault, J. A., Romans, B. W., Fildani, A., McGann, M., and Graham, S. A. (2010). Rapid climatic signal propagation from source to sink in a southern California sediment-routing system. *J. Geol.* 118, 247–259. doi: 10.1086/651539

Crouch, J. K., and Suppe, J. (1993). Late cenozoic tectonic evolution of the los angeles basin and inner california borderland: a model for core complex-like crustal extension. *Geol. Soc. Am. Bull.* 105, 1415–1434. doi: 10.1130/0016-7606(1993)105<1415:lcteot>2.3.co;2

Dartnell, P., Driscoll, N. W., Brothers, D., Conrad, J. E., Kluesner, J., Kent, G. M., et al. (2015). *Colored Shaded-Relief Bathymetry, Acoustic Backscatter, and Selected Perspective Views of the Inner Continental Borderland, Southern California*. US Geological Survey Scientific Investigations Map 3324. San Diego, CA: USGS.

DeMets, C., and Dixon, T. H. (1999). New kinematic models for pacific-north america motion from 3 Ma to present, I: evidence for steady motion and biases in the NUVEL-1A model. *Geophys. Res. Lett.* 26, 1921–1924. doi: 10.1029/1999gl900405

Eberhart-Phillips, D., and Bannister, S. (2010). 3-D imaging of Marlborough, New Zealand, subducted plate and strike-slip fault systems. *Geophys. J. Int.* 182, 73–96. doi: 10.1111/j.1365-246X.2010.04621.x

Ebuna, D. R., Mitchell, T. J., Hogan, P. J., Nishenko, S., and Greene, H. G. (2013). "High-resolution offshore 3D seismic geophysical studies of infrastructure geohazards," in *Proceedings of the Symposium on the Application of Geophysics to Engineering and Environmental Problems 2013*, (Denver: Society of Exploration Geophysicists and Environment and Engineering Geophysical Society), 311–320.

Edwards, J. H., Kluesner, J. W., Silver, E. A., and Bangs, N. L. (2018). Pleistocene vertical motions of the Costa Rican outer forearc from subducting topography and a migrating fracture zone triple junction. *Geosphere* 14, 510–534. doi: 10.1130/GES01577.1

Eriksen, F. N., Berndt, C., Karstens, J., and Crutchley, G. J. (2015). "P-cable high resolution 3D seismic-case study and recent advances," in *Proceedings of the Near-Surface Asia Pacific Conference*, Waikoloa, 116–119.

Fischer, P. J., and Mills, G. I. (1991). "The offshore newport-inglewood-rose canyon fault zone, California: structure, segmentation, and tectonics. environmental perils, San Diego region," in *Proceedings of the San Diego Association of Geologists for Geologic Society of America Meeting*, San Diego, CA, 17–36.

Freeman, S. T., Heath, E. G., Guptill, P. D., and Waggoner, J. T. (1992). Seismic hazard assessment, newport-inglewood fault zone. *Eng. Geol. Practice South. Calif.* 4, 211–231.

Grant, L. B., and Shearer, P. M. (2004). Activity of the offshore newport-inglewood rose canyon fault zone, coastal southern california, from relocated microseismicity. *Bull. Seismol. Soc. Am.* 94, 747–752. doi: 10.1785/0120030149

Grant, L. B., Waggoner, J. T., Rockwell, T. K., and von Stein, C. (1997). Paleoseismicity of the north branch of the newport-inglewood fault zone in huntington beach, California, from cone penetrometer test data. *Bull. Seismol. Soc. Am.* 87, 277–293.

Gulick, S. P., Bangs, N. L., Moore, G. F., Ashi, J., Martin, K. M., Sawyer, D. S., et al. (2010). Rapid forearc basin uplift and megasplay fault development from 3D seismic images of Nankai Margin off Kii Peninsula, Japan. *Earth Planet. Sci. Lett.* 300, 55–62. doi: 10.1016/j.epsl.2010.09.034

Hamling, I. J., Hreinsdóttir, S., Clark, K., Elliott, J., Liang, C., Fielding, E., et al. (2017). Complex multifault rupture during the 2016 Mw7.8 Kaikôura Earthquake, New Zealand. *Science* 356:eaam7194. doi: 10.1126/science.aam7194

Hauksson, E., and Gross, S. (1991). Source Parameters of the 1933 Long Beach Earthquake. *Bull. Seismol. Soc. Am.* 81, 81–98. doi: 10.1029/JB075i026p04997

Hill, M. (1971). Newport-inglewood zone and mesozoic subduction, California. *GSA Bull.* 82, 2957–2962. doi: 10.1130/0016-7606(1971)82[2957:nzamsc]2.0.co;2

Hogarth, L. J., Babcock, J., Driscoll, N. W., Le Dantec, N., Haas, J. K., Inman, D. L., et al. (2007). Long-term tectonic control on holocene shelf sedimentation offshore La Jolla, California. *Geology* 35, 275–278. doi: 10.1130/G23234a.1

Kaiser, A., Balfour, N., Fry, B., Holden, C., Litchfield, N., Gerstenberger, M., et al. (2017). The 2016 Kaikôura, New Zealand, earthquake: preliminary seismological report. *Seismol. Res. Lett.* 88, 727–739. doi: 10.1785/0220170018

Kalid, N. Z. A., Hamzah, U., and Samsudin, A. R. (2016). Seismic attributes and their application in faults interpretation of Kupe Field, Taranaki Basin, New Zealand. *Electron. J. Geotech. Eng.* 21, 1037–1052.

Kienast, S. S., and McKay, J. L. (2001). Sea surface temperatures in the subarctic northeast Pacific reflect millennial-scale climate oscillations during the last 16 kyrs. *Geophys. Res. Lett.* 28, 1563–1566. doi: 10.1029/2000GL012543

Klotsko, S., Driscoll, N., Kent, G., and Brothers, D. (2015). Continental shelf morphology and stratigraphy offshore San Onofre, California: the interplay between rates of eustatic change and sediment supply. *Mar. Geol.* 369, 116–126. doi: 10.1016/j.margeo.2015.08.003

Kluesner, J. W., and Brothers, D. S. (2016). Seismic attribute detection of faults and fluid pathways within an active strike-slip shear zone: new insights from high-resolution 3D P-Cable^{TM}? seismic data along the hosgri fault, offshore california. *Interpretation* 4, SB131–SB148. doi: 10.1190/INT-2015-0143.1

Kovanen, D. J., and Easterbrook, D. J. (2002). Paleodeviations of radiocarbon marine reservoir values for the northeast Pacific. *Geology* 30, 243–246. doi: 10.1130/0091-7613(2002)030<0243:pormrv>2.0.co;2

Kranz, R. L. (1979). Crack-crack and crack-pore interactions in stressed granite. *Int. J. Rock Mech. Mining Sci. Geomech.* 16, 37–47. doi: 10.1016/0148-9062(79)90773-3

Le Dantec, N., Hogarth, L. J., Driscoll, N. W., Babcock, J. M., Barnhardt, W. A., and Schwab, W. C. (2010). Tectonic controls on nearshore sediment accumulation and submarine canyon morphology Offshore La Jolla, Southern California. *Mar. Geol.* 268, 115–128. doi: 10.1016/j.margeo.2009.10.026

Legg, M. R. (1991). "Developments in understanding the tectonic evolution of the california continental borderland," in *From Shoreline to Abyss: Contributions in Marine Geology in Honour of Francis Parker Shepard*, ed. R. H. Osborne (Tulsa: SEPM Society for Sedimentary Geology).

Lindsey, E. O., and Fialko, Y. (2013). Geodetic slip rates in the southern san andreas fault system: effects of elastic heterogeneity and fault geometry. *J. Geophys. Res. Solid Earth* 118, 689–697. doi: 10.1029/2012JB009358

Lindvall, S. C., and Rockwell, T. K. (1995). Holocene activity of the rose canyon fault zone in San Diego, California. *J. Geophys. Res. Solid Earth* 100, 24121–24132. doi: 10.1029/95JB02627

Lonsdale, P. (1991). "Structural patterns of the Pacific floor offshore of Peninsular California," in *Gulf and Peninsular Province of the Califor- nias: American Association of Petroleum Geologists Memoir*, eds J. P. Dauphin and B. R. T. Simoneit (Tulsa: AAPG), 87–143.

Maloney, J. M., Driscoll, N. W., Kent, G. M., Bormann, J., Duke, S., and Freeman, T. (2016). "Segmentation and step-overs along strike-slip fault systems in the inner California borderlands: implications for fault architecture and Basin Formation," in *Applied Geology in California*, eds R. Anderson and H. Ferriz (New York, NY: Star Publishing), 655–677.

Mineral Management Service [MMS] (1997). *Oceanside Seismic Data. (set)*. Washington, DC: U.S. Department of the Interior.

Morley, C. K. (2018). 3-D seismic imaging of the plumbing system of the Kora Volcano, Taranaki Basin, New Zealand: the influence of syn-rift structure on shallow igneous intrusion architecture. *Geosphere* 14, 2533–2584. doi: 10.1130/GES01645.1

Morley, C. K., Maczak, A., Rungprom, T., Ghosh, J., Cartwright, J. A., Bertoni, C., et al. (2017). New style of honeycomb structures revealed on 3D seismic data indicate widespread diagenesis offshore Great South Basin, New Zealand. *Mar. Petrol. Geol.* 86, 140–154. doi: 10.1016/j.marpetgeo.2017.05.035

Nicholson, C., Sorlien, C. C., Atwater, T., Crowell, J. C., and Luyendyk, B. P. (1994). Microplate capture, rotation of the western transverse ranges, and initiation of the san-andreas transform as a low-angle fault system. *Geology* 22, 491–495. doi: 10.1130/0091-7613(1994)022<0491:mcrotw>2.3.co;2

Nishenko, S., Gary Greene, H., Hogan, P., and Bergkamp, B. (2018). Geometry and late pleistocene displacement of the shoreline and oceano fault zones, san luis obispo Bay, California. *Bull. Seismol. Soc. Am.* 108, 3225–3247. doi: 10.1785/0120160177

Normark, W. R., Piper, D. J., Romans, B. W., Covault, J. A., Dartnell, P., Sliter, R. W., et al. (2009). Submarine canyon and fan systems of the California Continental Borderland. *Earth Sci. Urban Ocean* 454, 141–168. doi: 10.1130/2009.2454(2.7)

Pacific Gas and Electric Company [PG & E] (2014). *Offshore Low-Energy Seismic Reflection Studies in Estero Bay, San Luis Obispo Bay, and Point Sal Areas*. PG&E Tech- nical Report, GEO.DCPP.TR.14.02. San Francisco, CA: Pacific Gas and Electric Company.

Platt, J. P., and Becker, T. W. (2010). Where is the real transform boundary in California? *Geochem. Geophys. Geosyst.* 11, 1–19. doi: 10.1029/2010GC003060

Roberts, A. (2001). Curvature attributes and their application to 3D interpreted horizons. *First Break* 19, 85–100. doi: 10.1046/j.0263-5046.2001.00142.x

Rockwell, T. K. (2010). "The rose canyon fault zone in San Diego," in *Proceeding of Fifth International Conference on Recent Advances in Geotechnical Earthquake Engineering and Soil Dynamics*, San Diego.

Roden, R., Smith, T., and Sacrey, D. (2015). Geologic pattern recognition from seismic attributes: principal component analysis and self-organizing maps. *Interpretation* 3, SAE59–SAE83. doi: 10.1190/INT-2015-0037.1

Ryan, H. F., Legg, M. R., Conrad, J. E., Sliter, R. W., Lee, H. J., and Normark, W. R. (2009). Recent faulting in the gulf of santa catalina: San Diego to dana point. *Earth Sci. Urban Ocean* 454, 291–315. doi: 10.1130/2009.2454(4.5)

Sahakian, V., Bormann, J., Driscoll, N., Harding, A., Kent, G., and Wesnousky, S. (2017). Seismic constraints on the architecture of the newport-inglewood/rose canyon fault: implications for the length and magnitude of future earthquake ruptures. *J. Geophys. Res. Solid Earth* 122, 2085–2105. doi: 10.1002/2016JB013467

Singleton, D. M., Rockwell, T. K., Murbach, D., Murbach, M., Maloney, J. M., Freeman, T., et al. (2019). Late-holocene rupture history of the rose canyon fault in old town, san diego: implications for cascading earthquakes on the newport–inglewood–rose canyon fault system. *Bull. Seismol. Soc. Am.* 109, 855–874. doi: 10.1785/0120180236

Southon, J. R., Nelson, D. E., and Vogel, J. S. (1990). A record of past ocean-atmosphere radiocarbon differences from the northeast Pacific. *Paleoceanography* 5, 197–206. doi: 10.1029/PA005i002p00197

Stirling, M. W., Litchfield, N. J., Villamor, P., Van Dissen, R. J., Nicol, A., Pettinga, J., et al. (2017). The Mw 7.8 2016 Kaikóura earthquake: surface fault rupture and seismic hazard context. *Bull. New Zeal. Soc. Earthq. Eng.* 50, 73–84. doi: 10.5459/bnzsee.50.2.73-84

Stuiver, M., and Pollach, H. (1977). On the reporting of 14C ages. *Radiocarbon* 19, 355–359.

Stuiver, M., and Reimer, P. J. (1993). Extended 14 C data base and revised CALIB 3.0 14 C age calibration program. *Radiocarbon* 35, 215–230. doi: 10.1017/S0033822200013904

Triezenberg, P. J., Hart, P. E., and Childs, J. R. (2016). *National Archive of Marine Seismic Surveys (NAMSS): A USGS data website of marine seismic reflection data within the U.S. Exclusive Economic Zone (EEZ)*. San Diego, CA: U.S. Geological Survey Data Release.

U.S. Geological Survey [USGS], and California Geological Survey [CGS] (2006). *Quaternary Fault and Fold Database for the United States*. Availbale at: http://earthquake.usgs.gov/hazards/qfaults/ (accessed September 12, 2019)

Wei, E. A., Holmes, J. J., and Driscoll, N. W. (2019). Strike-slip tectonics offshore san onofre, california inhibits sediment delivery to the deep sea. *Front. Earth Sci.* 8:51. doi: 10.3389/feart.2020.00051

Wells, D. L., and Coppersmith, K. J. (1994). New empirical relationships among magnitude, rupture length, rupture width, rupture area, and surface displacement. *Bull. Seismol. Soc. Am.* 84, 974–1002.

Wesnousky, S. G. (2006). Predicting the endpoints of earthquake ruptures. *Nature* 444, 358–360. doi: 10.1038/nature05275

Wessel, P., Smith, W. H., Scharroo, R., Luis, J., and Wobbe, F. (2013). Generic mapping tools: improved version released. *EOS Trans. Am. Geophys. Union* 9, 409–410. doi: 10.1002/2013EO450001

Conflict of Interest: The authors declare that the research was conducted in the absence of any commercial or financial relationships that could be construed as a potential conflict of interest.